

The effects of high density on the X-ray spectrum reflected from accretion discs around black holes

Javier A. García,^{1★} Andrew C. Fabian,^{2★} Timothy R. Kallman,³ Thomas Dauser,⁴
Michael L. Parker,² Jeffrey E. McClintock,¹ James F. Steiner⁵ and Jörn Wilms⁴

¹Harvard-Smithsonian Center for Astrophysics, 60 Garden St, Cambridge, MA 02138, USA

²Institute of Astronomy, Madingley Road, Cambridge CB3 0HA, UK

³NASA Goddard Space Flight Center, Code 662, Greenbelt, MD 20771, USA

⁴Remeis Observatory and ECAP, Universität Erlangen-Nürnberg, Sternwartstr. 7, D-96049 Bamberg, Germany

⁵MIT Kavli Institute for Astrophysics and Space Research, MIT, 70 Vassar Street, Cambridge, MA 02139, USA

Accepted 2016 July 12. Received 2016 July 5; in original form 2016 March 28

ABSTRACT

Current models of the spectrum of X-rays reflected from accretion discs around black holes and other compact objects are commonly calculated assuming that the density of the disc atmosphere is constant within several Thomson depths from the irradiated surface. An important simplifying assumption of these models is that the ionization structure of the gas is completely specified by a single, fixed value of the ionization parameter ξ , which is the ratio of the incident flux to the gas density. The density is typically fixed at $n_e = 10^{15} \text{ cm}^{-3}$. Motivated by observations, we consider higher densities in the calculation of the reflected spectrum. We show by computing model spectra for $n_e \gtrsim 10^{17} \text{ cm}^{-3}$ that high-density effects significantly modify reflection spectra. The main effect is to boost the thermal continuum at energies $\lesssim 2 \text{ keV}$. We discuss the implications of these results for interpreting observations of both active galactic nuclei and black hole binaries. We also discuss the limitations of our models imposed by the quality of the atomic data currently available.

Key words: accretion, accretion discs – atomic processes – line: formation – radiative transfer – relativistic processes – X-rays: general.

1 INTRODUCTION

X-ray reflection spectroscopy is arguably the most effective means currently available for probing the effects of strong gravity near the event horizon of an accreting black hole. The reflection spectrum is produced from the reprocessing of high-energy coronal photons in an optically thick accretion disc. The result is a rich spectrum of radiative recombination continua, absorption edges and fluorescent lines, most notably the Fe K complex in the 6–8 keV energy range (Ross & Fabian 1993; Rózańska et al. 2002; García & Kallman 2010). This reflected radiation leaves the disc carrying a wealth of information on the physical composition and condition of the matter in the strong field near a black hole. The Fe K emission lines (and other fluorescent lines) are broadened and shaped by Doppler effects, light bending and gravitational redshift (Fabian et al. 2000; Reynolds & Nowak 2003; Dovčiak, Karas & Yaqoob 2004; Dauser et al. 2012).

Reflection models are the *sine qua non* of the Fe-line method of measuring black hole spin, which is enormously important because

of its dominant role in measuring the spins of supermassive black holes in active galactic nuclei (AGN; e.g. Patrick et al. 2011; Walton et al. 2013; Parker et al. 2014; Reynolds 2014). Importantly, this method is equally applicable to measuring the spins of stellar-mass black holes (i.e. black hole binaries, BHB; Gou et al. 2014; McClintock, Narayan & Steiner 2014; Steiner et al. 2014; Chen et al. 2015; Miller & Miller 2015). X-ray reflection is also observed in other astrophysical sources such as neutron stars (Cackett et al. 2010), cataclysmic variables (Mukai et al. 2015), and ultracompact X-ray binaries (Madej et al. 2014).

For the past three decades, models of X-ray reflection, which are complex, have undergone continual improvement (see Fabian & Ross 2010, for a review). Currently, the most advanced model is `XILLVER`, which, relative to earlier models, incorporates a more complete atomic data base and an improved solution to the problem of radiative transfer (García & Kallman 2010; García et al. 2013). The reflection model `XILLVER` has been linked with the relativistic convolution code `RELLINE` (Dauser et al. 2010, 2013) to provide the complete relativistic reflection package `RELXILL` (García et al. 2014), which is presently the state of the art in modelling-ionized reflection in strong gravity. As the wealth of observational data grows in both quantity and quality, so must the theoretical models.

* E-mail: javier@head.cfa.harvard.edu (JAG); acf@ast.cam.ac.uk (ACF)

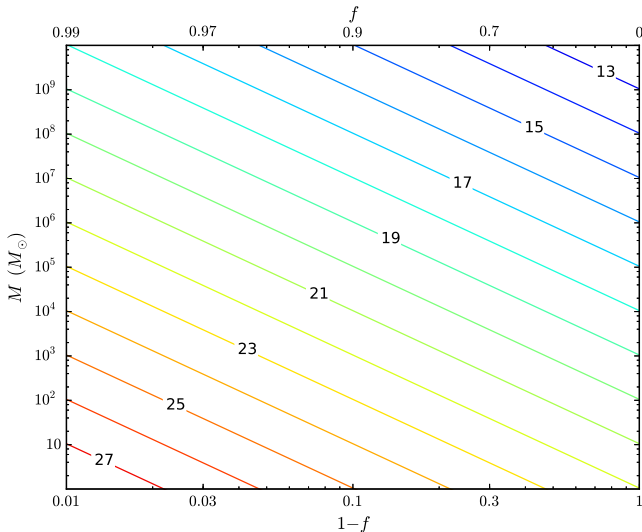


Figure 1. Black hole mass versus coronal power based on the radiation pressure solution from Svensson & Zdziarski (1994). Lines show constant $n_e \dot{m}^2$ for different values of the density, as indicated, and assuming $r = 10$ and $\alpha = 0.1$. For a 10 solar mass black hole at the minimum f , the density is still near 10^{22} cm^{-3} .

A common simplifying assumption of reflection models is that the density of the disc atmosphere is constant, although hydrostatic atmosphere models have been explored (e.g. Ballantyne, Ross & Fabian 2001; Nayakshin & Kallman 2001; Rózańska & Madej 2008). The assumption of constant density significantly simplifies the problem and so far has proven to provide a good representation of the data. A second simplification for constant density calculations is that a specific model can be characterized by a single value of the ionization parameter, which is proportional to the ratio of the illuminating flux to the gas density. In photoionization calculations, it is standard practice to assume that, for all values of flux and density under consideration, the ionization structure of the gas is solely determined by this one parameter. That is, it is simply the ratio of flux to density that determines the ionization structure of the atmosphere and properties of the reflection spectrum.

The effects of high density on the reflection spectrum are most important for powerful coronae and for black holes of low mass. Some high-density models ($n_e = 10^{20} \text{ cm}^{-3}$) for black hole binaries were computed by Ross & Fabian (2007), and for neutron stars by Ballantyne (2004). An equation relating the density of a standard α -disc at high-accretion rates, for which the inner region is radiation pressure-dominated, is given by Svensson & Zdziarski (1994):

$$n_e = \frac{1}{\sigma_T R_S} \frac{256\sqrt{2}}{27} \alpha^{-1} r^{3/2} \dot{m}^{-2} [1 - (3/r)]^{-1} (1-f)^{-3}, \quad (1)$$

where f is the fraction of the total power released into the corona; $\sigma_T = 6.64 \times 10^{-25} \text{ cm}^2$ is the Thomson cross-section; $R_S = 2GM/c^2$ is the Schwarzschild radius, $r = R/R_S$; and $\dot{m} = \dot{M}c^2/L_{\text{Edd}}^{-1}$ is the dimensionless accretion rate expressed in terms of the Eddington luminosity $L_{\text{Edd}} \sim 10^{38} \text{ erg s}^{-1}$. Fig. 1 shows, in the M versus f plane, lines of constant $n_e \dot{m}^2$ for $r = 10$ and $\alpha = 0.1$. Note that the pressure-dominated radius disappears when f approaches unity and when $\dot{m} < 0.1$, i.e. below 1 per cent of the Eddington limit (see fig. 2 of Svensson & Zdziarski 1994).

Most current reflection models adopt a moderate value of density, typically $n_e = 10^{15} \text{ cm}^{-3}$ or lower (e.g. Ross, Weaver & McCray 1978; Ross 1979; Ross & Fabian 1993; Zycki et al. 1994; Dumont

et al. 2003; Ross & Fabian 2005; García & Kallman 2010; García, Kallman & Mushotzky 2011; García et al. 2013, 2014), which is appropriate for low values of the coronal fraction f , high mass accretion rates, and black holes with $M > 10^7 M_\odot$. Meanwhile, for lower accretion rates and low-mass black holes, current models should be adequate because, as we shall demonstrate, the major effects of higher densities on the reflection spectrum occur below 3 keV.

In this paper, using the `XILLVER` code and the approximation of constant density, we explore the effects on reflection spectra of varying the gas density over the range $n_e = 10^{15} - 10^{19} \text{ cm}^{-3}$. We show that the temperature of the atmosphere increases markedly at $n_e \gtrsim 10^{17} \text{ cm}^{-3}$. The main effect on the spectrum is a significant increase in the flux at low energies ($\lesssim 2 \text{ keV}$).

This paper is organized as follows. In Section 2, we describe in detail the effects of high density on the thermal and ionization balance, and hence on models of the reflection spectrum. In Section 3, we discuss the implications of these effects for modelling AGN and BHB spectral data, as well as the limitations of the models themselves that are imposed by the quality of the atomic data currently available.

2 X-RAY REFLECTION AT HIGH-DENSITY

The calculations of the reprocessing of X-rays in illuminated accretion discs are carried out using our reflection code `XILLVER`. This approach has been extensively described in previous papers (García & Kallman 2010; García et al. 2013, 2014), therefore here we will only provide a short overview. `XILLVER` solves the radiative transfer in a plane-parallel (slab) geometry, using the Feautrier method as described in Mihalas (1978). The boundary condition at the surface of the disc, which is placed at a Thomson depth $\tau_T = 10^{-4}$, specifies the incident radiation field. A second inner boundary condition specifies the incident radiation field at the bottom of the slab, which in our calculations is set at $\tau_T = 10$. The calculation of the ionization and thermal balance is done implementing the photoionization routines from the `XSTAR` code (Kallman & Bautista 2001), which incorporates the most complete atomic data base for modelling synthetic photoionized X-ray spectra. The microphysics captured by `XILLVER` is much more detailed than for any earlier code, principally because we treat in detail the K -shell atomic properties of many astrophysically relevant ions (e.g. Kallman et al. 2004; García et al. 2005, 2009).

An important simplification commonly adopted in reflection modelling is that the number density n_e in the illuminated atmosphere (which sits on top of a much more optically thick, geometrically thin accretion disc), is constant. This simplification is motivated by the need for large grid of models that can be easily applied to real observational data. Moreover, this has proven to be sufficient to accurately describe the reflected spectrum. Similar calculations have been performed assuming that the atmosphere is in hydrostatic equilibrium (e.g. Ballantyne et al. 2001; Nayakshin & Kallman 2001). However, while such calculations are much more complex than those for constant density, it is still unclear whether the hydrostatic approximation provides a solution significantly closer to reality than a constant density calculation. In this paper, we do not seek to discuss the trade-off between different approximations. For the remainder, we will focus on exploring the effects of high density in X-ray-illuminated atmospheres with constant density.

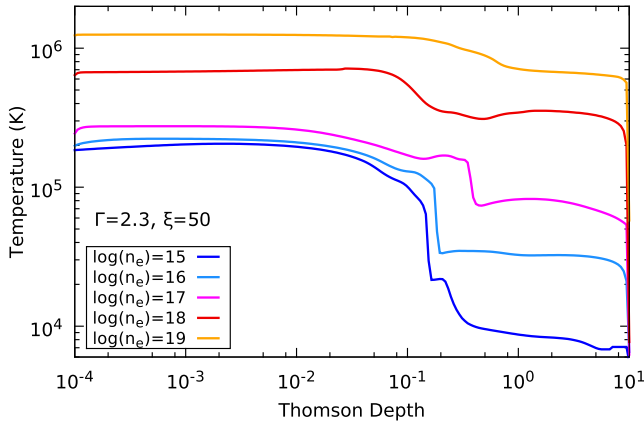


Figure 2. Temperature profiles in the vertical direction of the illuminated atmosphere. Each curve corresponds to a different value of density, as indicated, while the ionization parameter is held constant at $\xi = 50 \text{ erg cm s}^{-1}$. Other model parameters are: $\Gamma = 2.3$, $E_{\text{cut}} = 300 \text{ keV}$, and $A_{\text{Fe}} = 1$.

A useful quantity to describe constant density models is the ionization parameter:

$$\xi = \frac{4\pi F_x}{n_e}, \quad (2)$$

where F_x is the ionizing flux in the 1–1000 Ry band. This quantity is typically taken as an indicator of the degree of ionization in the material. This is because it is a measure of the ratio of the photoionization rate (which is proportional to $F_x \times n_e$) to the recombination rate (which is proportional to n_e^2). Thus, in photoionization modelling of constant density plasmas, it is normally assumed that the ξ completely characterizes each model, regardless of the actual values of density or flux. From this, it is clear that the assumption that both density and flux can be characterized by a single quantity ξ is valid as long as photoionization and recombination are the dominant processes controlling the thermal and ionization balance of the gas. However, as we show next, this assumption is invalid at sufficiently high densities, as other physical processes become important.

2.1 Temperature solutions

To explore the effects of high density on the reflected spectra, we have carried out calculations with `XILLVER` for various values of the density while keeping the ionization parameter constant. For all these models, the illumination is described as a power-law spectrum with slope $\Gamma = 2.3$, with a sharp low-energy cutoff at 0.1 keV and a high-energy exponential roll-over at 300 keV. The abundances of all elements are set to their solar values. These parameters are typical for AGN or BHB in the soft state. The density is varied in the $n_e = 10^{15}–10^{19} \text{ cm}^{-3}$ range, and the net incident flux is also varied such that the ionization parameter is always $\xi = 50 \text{ erg cm s}^{-1}$.

Fig. 2 shows the temperature profiles in the vertical direction of the illuminated slab resulting from models with five different densities (as indicated). The overall profiles follow closely the expected behaviour in a constant density photoionized slab: the temperature is higher at the illuminated surface ($\tau_T = 10^{-4}$) where the gas is more ionized. At larger depths, as enough photons are removed from the ionizing continuum, the gas recombines and the temperature decreases rapidly. This two-zone profile has been reported in

several previous reflection calculations (e.g. Ross & Fabian 2005; García & Kallman 2010; García et al. 2013).

The temperature tends to increase with the increase in density. For densities in the $15 < \log(n_e) < 17$ range, the hot zone of the slab shows modest variation, while in the deeper zones, the temperature rises with density. For higher densities, the temperature increase can be observed everywhere in the atmosphere. At each point, the temperature is determined by the balance of Compton heating and cooling, free–free heating and cooling, photoionization heating, and radiative recombination cooling.

Because of its quadratic dependence on the density, free–free (bremsstrahlung) heating–cooling is expected to be the dominant process leading temperature changes. Another major effect of high densities is the enhancement of the collisional de-excitation, which in turn suppresses radiative cooling, thus raising the temperature. Additionally, three-body recombination becomes important at $\log(n_e) \sim 19$, which lowers the ionization state. Lower ionization translates into larger photoionization heating.

All the relevant heating and cooling rates for the models mentioned above are plotted in Fig. 3. Since we are comparing models with the same ξ , a larger density implies a larger flux. A larger flux increases the photoionization as well as the Compton heating. However, these two rates depend linearly on density, while the free–free heating has an n_e^2 dependence. Compton heating and cooling scale with $n_e F_x$ independently of the ionization or temperature, but their contribution is small compared to the others. The bremsstrahlung cooling has an explicit dependence with the temperature, thus its behaviour is quite similar to that seen in Fig. 2. For $\log(n_e) = 15–17$, the free–free heating becomes dominant only in the inner part of the atmosphere, at large τ_T . At the surface, photoionization heating is the leading process.

Finally, in all the temperature profiles, a rather sharp decrease is seen near the inner boundary at $\tau_T = 10$. This is due to the boundary condition: there is a zero incident radiation field at the inner boundary. This setting is somewhat inconsistent with the picture of an illuminated atmosphere seated atop a relatively cold disc. However, we have found through extensive numerical tests that unless the incident radiation field is quite strong, the particular choice of the boundary condition at such large depths is inconsequential to the output-reflected spectrum.

2.2 Reflected spectra

The reflected spectra corresponding to the temperature solutions discussed in Section 2.1 are shown in Fig. 4. For simplicity, we show the angle-averaged emitted spectrum at the surface of the illuminated disc. Each curve is normalized by an extra factor in flux with respect to the model for $\log(n_e) = 15$ such that all the continua are placed at the same level (see the figure caption for details). The incident power-law spectrum is also shown. While all the spectra are similar at high energies ($\gtrsim 5 \text{ keV}$), they show increasing divergence at low energies.

The thermal part of the spectra at low energies follows the evolution of the temperature at the illuminated zone of the atmosphere. For the three lowest densities, there are not significant changes in the observable X-ray band ($\sim 0.1–200 \text{ keV}$). However, for $\log(n_e) = 18$ and above, the changes are dramatic. At 1 keV, there is almost one order of magnitude of difference in the reflected flux. This increased emission at soft energies agrees with the results first reported by Ballantyne (2004) in the context of neutron stars. The changes in the Fe K region are minor, although we note the suppression of the

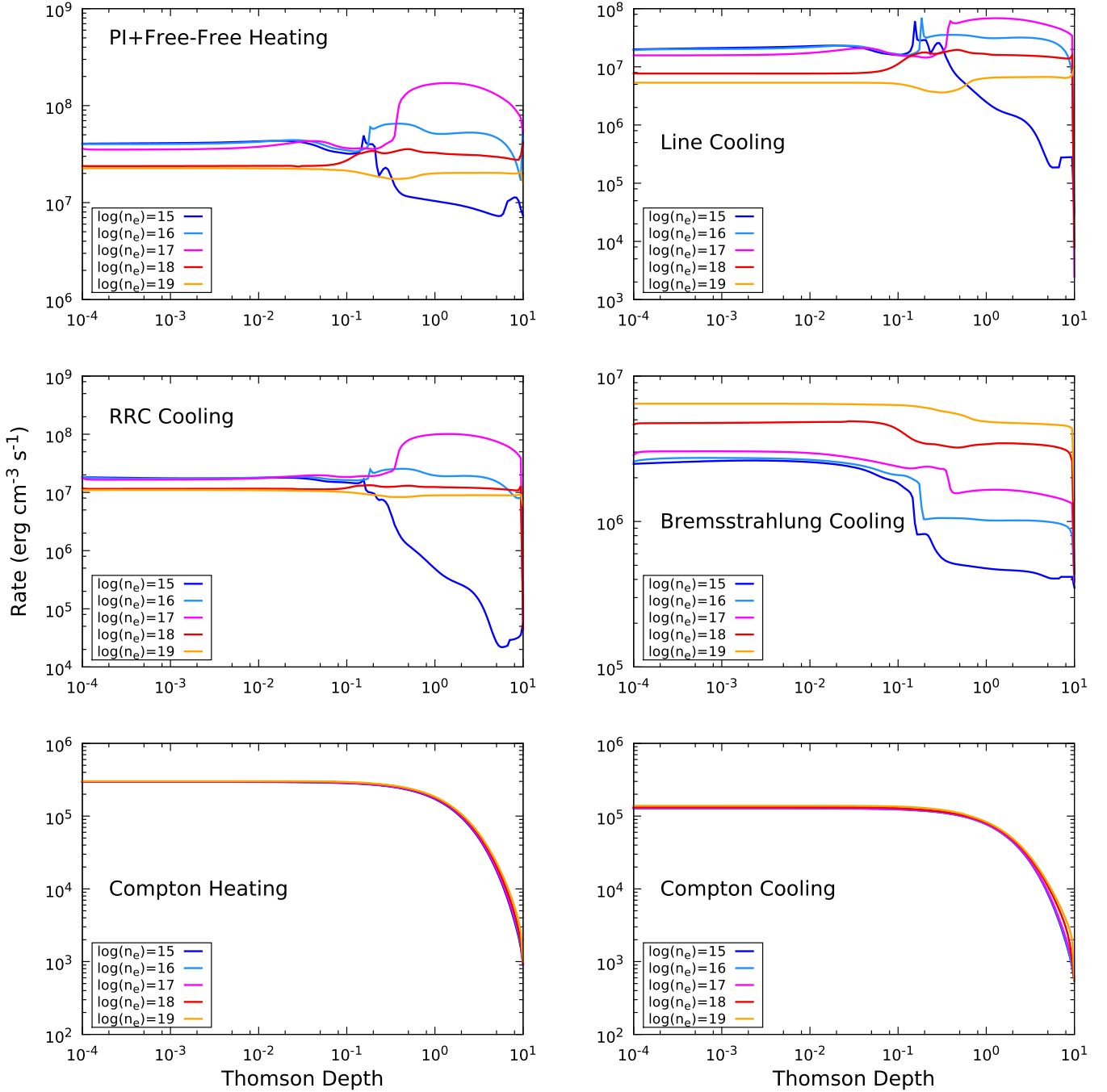


Figure 3. Various heating and cooling rates included in the reflection calculations shown in Fig. 2. Each curve is normalized in amplitude to match the extra factor in flux and density with respect to the $\log(n_e) = 15$ case. Thus, the curves for $\log(n_e) = 16, 17, 18$ and 19 are divided by $10^2, 10^4, 10^6$ and 10^8 .

K β emission for the highest densities, which indicates a higher ionization state.

Notably, the higher density models give a soft excess which is much larger than for low density. The main effect is that as the density rises, the bremsstrahlung absorption in the outer layers becomes increasingly important at lower energies. In the regions where free-free absorption is the dominant source of opacity, the gas radiates like a blackbody at the local temperature T . Thus, at low energies ($E \ll kT$), the emitted spectrum follows the Rayleigh–Jeans law $I \propto E^2$ (Felten & Rees 1972), causing the surface temperature to increase.

Consider the free-free absorption coefficient for $E \ll kT$, given by

$$\chi_{\text{ff}} = 7.34 \times 10^{-20} n_e^2 g T^{-3/2} E^{-2}, \quad (3)$$

where g is the temperature-averaged Gaunt factor. The energy E^* at which the free-free equals the Thomson opacity $\chi_{\text{T}} = n_e \sigma_{\text{T}}$ (where $\sigma_{\text{T}} = 6.65 \times 10^{-25} \text{ cm}^2$ is the Thomson cross-section) can be written as

$$E^* = \sqrt{7.34 \times 10^{-20} n_e g T^{-3/2} \sigma_{\text{T}}^{-1}}, \quad (4)$$

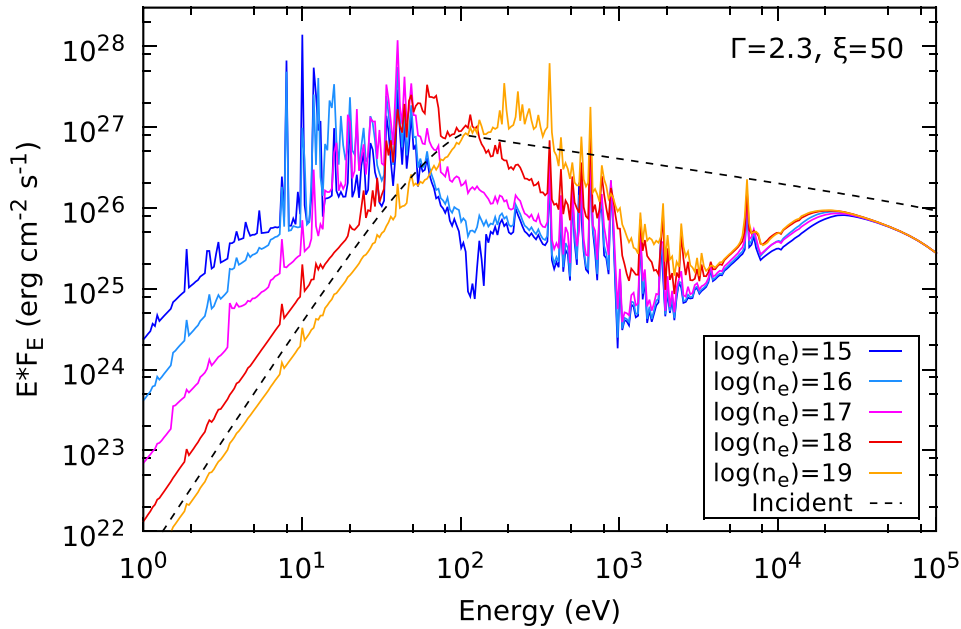


Figure 4. Angle-averaged reflected spectra for the same models shown in Fig. 2. The solid curves correspond to the density values indicated in the legend. The dashed curve is the incident power-law spectrum that illuminates the disc, and it is the same for all models. Each curve is normalized by an extra factor in flux with respect to the model for $\log(n_e) = 15$. This factor is 10, 10^2 , 10^3 and 10^4 for models with $\log(n_e) = 16, 17, 18$ and 19 , respectively.

In the non-relativistic limit, we may approximate $g \approx 1$. Because the temperature in the illuminated region of the slab is fairly constant, we can evaluate the expression above for single values of density and temperature. Looking at the region for $\tau_T \lesssim 0.01$ in the profiles of Fig. 2, we find $E^* = 0.05, 0.1, 0.4, 0.8$ and 2 keV for $\log(n_e) = 15-19$, respectively. For all energies below E^* , χ_{H} is the dominant opacity. Note that these energies are approximate, and in fact for energies above ~ 0.1 keV, the photoelectric opacity from the various metals becomes important. However, this simple derivation explains the Rayleigh–Jeans shape of the reflected spectrum at low energies.

The relatively strong absorption near 100 eV observed in the spectra for $\log(n_e) = 15$ is due to cluster of resonance lines from O V, O VI and Ne VIII, which blend together with the absorption edges from O IV (~ 77 eV), Ne IV (~ 97 eV) and O V (~ 113 eV). Meanwhile, the absorption near 1 keV seen in almost all spectra is due to the K edge of O VII.

The lowest density models predict strong emission lines in the $\sim 5-100$ eV range. These are the Lyman series of H, as well as the UV resonance lines of C IV, N V and O VI (some below 10 eV). Above 13.6 eV are the resonance lines of all the trace elements plus He II (304 Å), He I (584 Å) and the coronal lines of Fe near 60–70 eV. However, the 13.6–100 eV region is unobservable due to absorption in the Galactic interstellar medium. Strong lines below 13.6 eV (such as H Ly α) should be observable in UV spectra, but disc rotation will presumably broaden these lines, rendering them unobservable. In addition, other emission components such as the ‘Big Blue Bump’ (BBB), a broad emission that peaks in the UV (Sanders et al. 1989; Elvis et al. 1994), will further reduce their equivalent width – coincidentally, the BBB itself has been attributed to blurred reprocessed radiation from fast moving clouds (e.g. Lawrence 2012). Finally, if the disc’s covering fraction is lower than ~ 0.1 , then the classic UV broad lines

typically observed in AGN will be stronger than the disc reflection lines.

The differences observed in the reflected spectra are a direct consequence of the effects of high density in the ionization balance of the illuminated atmosphere. This is illustrated in Fig. 5, where we plot the ionic fractions for H and all ions of H, O, and Fe (the most abundant elements), for three of the calculations presented above, namely for those with $\log(n_e) = 15, 17$ and 19 . The evolution in the ionization structure with increasing density is quite evident.

At $\log(n_e) = 15$ (upper panels of Fig. 5), H and He are fully ionized in the illuminated hot region near the surface, and then recombine at a small depth ($\tau_T \sim 0.1$), which is the region where the temperature drops most rapidly (Fig. 2). This transition is followed by other ions. H-like oxygen is dominant in most of the hot region, while neutral O dominates in the colder region. Likewise, Fe XVIII and Fe XIX are present near the surface, while deep inside only Fe II and Fe III are observed. This structure is dramatically changed at higher densities. For $\log(n_e) = 17$, the inner regions are dominated by O IV, Fe V and Fe VI. At $\log(n_e) = 19$, oxygen is fully ionized in the entire slab, while the lowest ionization stages of iron are Fe XVII, Fe XVI and Fe XV. These changes in ionic fractions affect both the photoelectric opacity and line emission, which has direct impact on the emitted spectrum. In general, higher density results in a hotter and more ionized atmosphere.

The results presented in this section are particularly relevant for narrow-line Seyfert 1 galaxies (e.g. 1H 0707–495, Section 3.2, for which the power-law continuum is observed to be steep). However, the typical index for an AGN is $\Gamma \sim 2$. Nevertheless, the high-density effects described above are still present when the incident continuum is flat. The main difference is that the soft-energy excess is slightly less pronounced in comparison to the soft-illumination case ($\Gamma = 2.3$). We notice, however, that for a

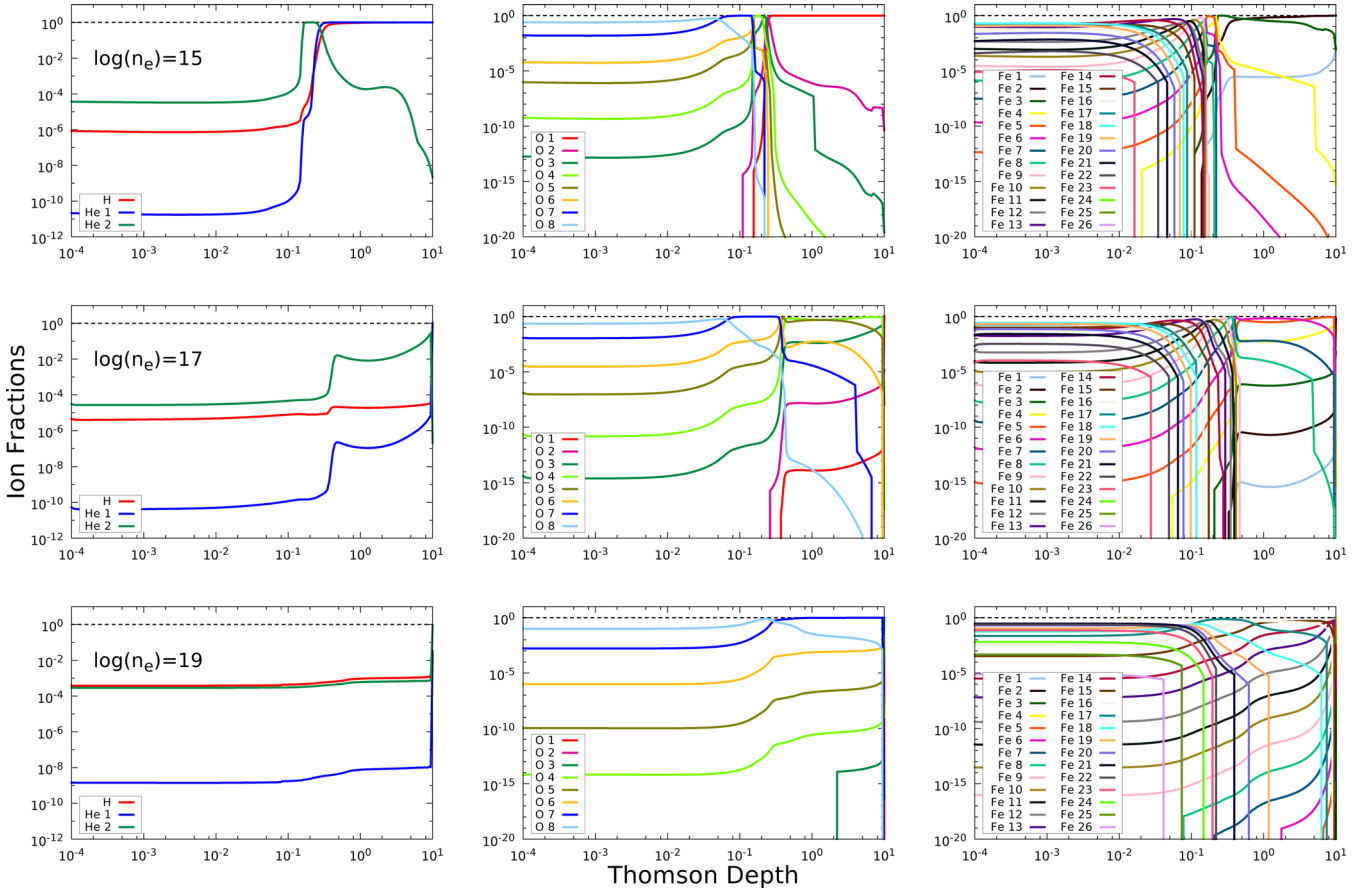


Figure 5. Fractions of the most abundant ions in the reflection calculations for $\log(n_e) = 15, 17$ and 19 . Left-hand panels show the fractions of H, He and He II (labelled as He 2 in the figure). Middle panels show the fractions of O ions, while right-hand panels show those for all Fe ions.

much harder continuum, the differences are very significant, as we describe in Section 3.3 for the case of $\Gamma = 1.6$.

3 DISCUSSION

3.1 Observational implications for AGN

We have shown in Section 2 that high-density effects are very important in the calculation of X-ray reflected spectra. The net result is a very significant increase in the continuum flux at energies below ~ 2 keV. This effect could have important observational implications. For example, the observed X-ray spectrum from many AGN often presents an emission excess at ~ 1 keV, referred to as the soft-excess (Turner & Pounds 1988). The nature of this emission is still a matter of debate. Possible explanations include Comptonized emission (Titarchuk 1994), reflection-reprocessed emission (Vasudevan et al. 2014) or complex absorption (Sobolewska & Done 2007). The calculations presented in this paper suggest that the soft-excess could be a measure of the density in the accretion disc, which provides a great diagnostic tool. For example, estimates of the density in the accretion disc can provide information on the black hole mass, given the relationship described in Section 1 (see in particular Fig. 1). However, a full exploration of the possible model degeneracies will be required before strong conclusions can be drawn.

High-density effects are also important in extreme cases where the illuminating source is very close to the black hole, which

enhances the reflection signal (Dauser et al. 2014). Recently, Kara et al. (2015) analysed *NuSTAR* and *XMM-Newton* observations of the narrow-line Seyfert I galaxy 1H0707-495. Fits using the RELXILLP model (i.e. relativistic reflection under a lamp-post geometry), constrained the height of the corona to be roughly $2r_g$ (where $r_g = GM/c^2$ is the gravitational radius), and a large reflection fraction $R_f > 5.8$, which indicates a very strong illumination. However, the ionization parameter was found to be moderate (between $\log \xi = 0.3$ and $\log \xi = 2$ depending on the data set analysed), which can only be explained by the density being high. Using the observed luminosity and the given ionization parameter, Kara et al. estimated a density of $n_e \sim 10^{17} \text{ cm}^{-3}$.

3.2 A simple test on 1H0707-495

In order to test the impact of high-density reflection models in fitting observational data, we have performed a simple analysis of one observation of 1H0707-495. We used the ~ 500 ks exposure from the *XMM-Newton* observation of the source collected between 2008 January 29 and February 6, using only the European Photon Imaging Camera-pn (Strüder et al. 2001). This is same observation analysed by Dauser et al. (2012), where the details on the data reduction are provided.

Additionally, we have produced a full grid of reflection models for high-density atmospheres with our code XILLVER. Given the very large number of calculations required, we only produced models for a gas density of $n_e = 10^{19} \text{ cm}^{-3}$ (i.e. the largest value considered

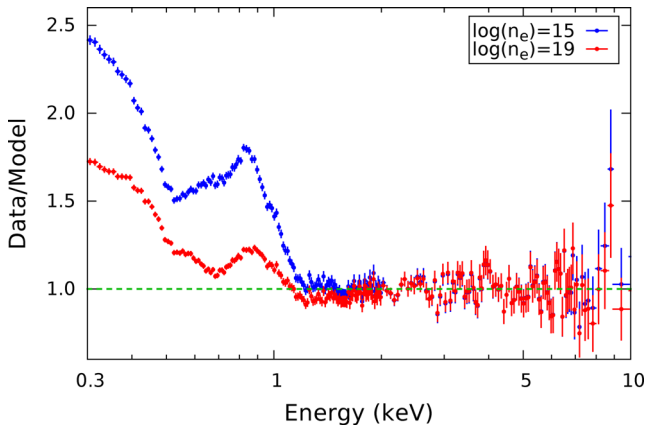


Figure 6. Ratio plots of the fits to the *XMM-Newton* data of 1H0707-495, using the relativistic reflection model `RELXILL` for $\log(n_e) = 15$ (blue points), and for $\log(n_e) = 19$ (red points). Only the 2–10 keV band is actually fitted, while the soft energies are included after the fit to illustrate the impact of the high-density model in that spectral band.

in the discussion of Section 2), with a high-energy cutoff fixed at 300 keV. The final grid of models contains a total of 9000 spectra covering a wide range of parameters: the slope of the illuminating power law ($1.2 \leq \Gamma \leq 3.4$), the Fe abundance in solar units ($0.5 \leq A_{\text{Fe}} \leq 20$), the ionization parameter ($0 \leq \log \xi \leq 4.7$) and the inclination ($5 \leq i \leq 89$).

The spectrum of 1H0707-495 has been previously analysed by several authors (e.g. Fabian et al. 2009; Zoghbi et al. 2010; Dauser et al. 2012; Kara et al. 2015). In general, the spectrum is found to be dominated by reflection, with a power-law continuum much steeper than generally found in AGN ($\Gamma \lesssim 3$). Surprisingly, the Fe abundance is always required to be supersolar, with values as large as 10–20 times the solar value. Most fits require either a strong thermal component (in the form of a blackbody), or two different reflection components. Given all these complexities, we do not seek to provide yet another detailed analysis of this peculiar source, but rather to use it as a simple test case for the high-density reflection models.

Therefore, we start by fitting the 2–10 keV energy band with a power-law continuum plus relativistically smeared reflection (both components provided by our model `RELXILL`). In addition, the model includes Galactic absorption (modelled with `Tbabs`), intrinsic absorption at the redshift of the source (modelled with `zTbabs`, with $z = 0.0411$). We perform two fits, one with the standard `XILLVER` grid (i.e. calculated with $n_e = 10^{15} \text{ cm}^{-3}$), and one with the high-density grid ($n_e = 10^{19} \text{ cm}^{-3}$). Both models provide a reasonably good fit for the data, with a reduced chi-square of $\chi^2_{\nu} = 1.31$ and 1.28 for the low- and high-density models, respectively, with all parameters between the two models consistent within their uncertainties. In particular, the Fe abundance is found to be supersolar ($A_{\text{Fe}} \sim 10$) with both models.

We then include the soft-energy data (i.e. the 0.3–2 keV region), without re-fitting. Fig. 6 shows the data-to-model ratio plot in these two cases. Interestingly, the high-density model makes a huge improvement in the soft band, decreasing the statistics from $\chi^2_{\nu} = 629.3$ for the low-density model, to $\chi^2_{\nu} = 215.4$ for the high-density model. Meanwhile, there is virtually no effect in the 2–10 keV region.

An obvious question arises from this analysis: will an even higher density improve further the fit of the soft energies? Unfortunately, limitations in the current atomic data prevent us from producing models at densities above $\log(n_e) \sim 18$ –19. This issue is further discussed in Section 3.4.

3.3 Observational implications for BHB

We have discussed so far calculations appropriate for the modelling of the X-ray reflection spectrum of AGN, i.e. steeper continua ($\Gamma \sim 2$) and relatively low ionization ($\log \xi \sim 0$ –2). Nevertheless, relativistic reflection is also commonly observed in the spectra of many BHB (e.g. García et al. 2015; Miller & Miller 2015; Parker et al. 2015), which in general show a harder continuum and a higher ionization parameter ($\log \xi \gtrsim 3$).

Fig. 7 shows the resulting temperature profiles and reflected spectra for models with $\Gamma = 1.6$ and $\xi = 10^3 \text{ erg cm s}^{-1}$. All other parameters are the same as those for the models presented in Section 2 (Figs 2 and 4). The effects of high density are less prominent at higher ionization. The temperature near the surface remains fairly constant regardless of the density, most likely because all elements are fully stripped and line cooling is already suppressed (unlike the case for low ξ). The temperature in the inner regions rises with density, due to the increase of the free–free heating, just as in the low-ionization models. Once again, the most significant effect in the reflected spectra (right-hand panel) is the modification of the Rayleigh–Jeans domain of the emission at soft energies. The most prominent features are the O Ly α line at ~ 0.8 keV, and the Fe K -shell emission at ~ 6.7 keV. The continuum between these two features grow with increasing density due to the reduction of the photoelectric opacity. However, the overall shape of the spectrum above ~ 1 keV is very similar among all models.

In the standard α -disc model (Shakura & Sunyaev 1973), the mid-plane density of the accretion disc around a stellar-mass black hole is a few orders of magnitude larger than in a disc around a supermassive black hole, simply because the density scales proportional to $m^{-1}r^{3/2}$, where m is the black hole mass and r the radius. Moreover, estimates of the gas density using multidimensional magnetohydrodynamic simulations can produce mid-plane densities $\gtrsim 10^{20} \text{ cm}^{-3}$ for a $10 M_{\odot}$ black hole accreting at 10 per cent the Eddington luminosity (e.g. Noble, Krolik & Hawley 2010; Schnittman, Krolik & Noble 2013).

In the soft and intermediate states, the power-law continuum is steep and a strong thermal disc component dominates X-ray spectrum, which, in some cases, makes the detection of the reflection signatures challenging. However, in the hard state, the thermal emission becomes faint and the spectrum is characterized by a harder ($\Gamma < 2$) power-law continuum with a high-energy cutoff. This continuum can typically be well described by Comptonization of soft thermal disc photons in a hot, optically thin corona. Many sources show clear reflection features in the hard state.

In some cases, a weak and relatively cold disc ($T \sim 0.2$ keV) component has been found in the hard-state spectra of some sources (e.g. GX 339-4; Reis et al. 2008; Plant et al. 2015). While the high-density effects appear to be milder in BHB models than in those for AGN, we do not discount the possibility that the faint soft emission observed in some BHB is due to a high-density reflector. A detailed analysis of these new models confronted with real observational data is required to answer this question, but outside the scope of this paper. Moreover, as discussed above, densities even larger than ones covered in the present calculations might be more appropriate to correctly represent the physics near stellar-mass black holes.

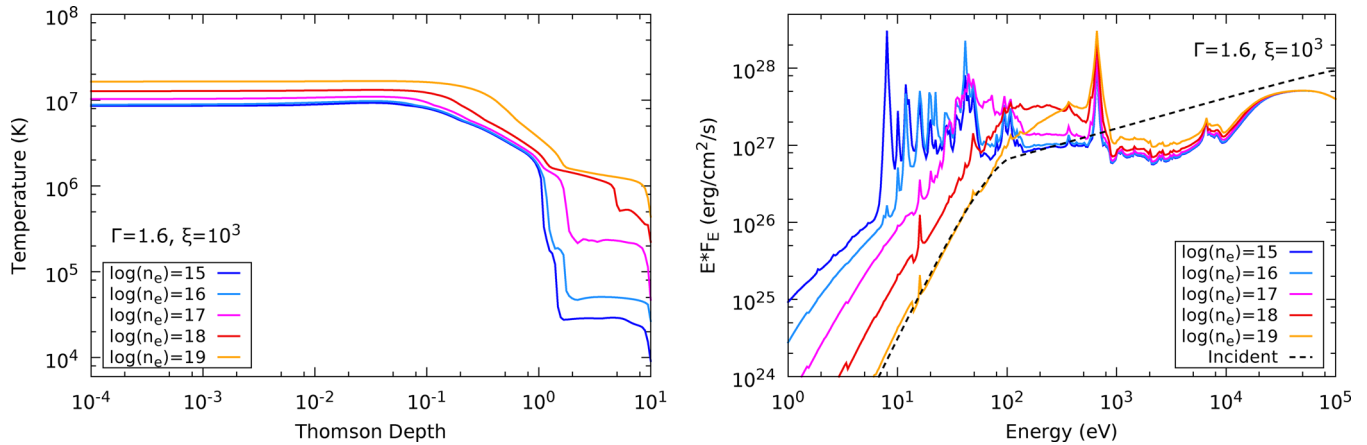


Figure 7. Reflection calculations for various densities (as indicated) using parameters appropriate for BHB, i.e. $\Gamma = 1.6$, $\log \xi = 3$, A_{Fe} and $E_{\text{cut}} = 300$ keV. (Left) Temperature profiles in the vertical direction of the disc. (Right) Angle-averaged reflected spectra. The curves are rescaled for clarity as in Fig. 4.

Such calculations are currently infeasible due to the lack of proper atomic data (see Section 3.4).

3.4 Limitations of the atomic data

The *XILLVER* reflection calculations presented here make use of the subroutines of the photoionization code *XSTAR* (Kallman & Bautista 2001), as well as its atomic data base (Bautista & Kallman 2001). These are used for the calculation of the ionization and thermal balance, plus line and continuum emissivities and opacities. While *XSTAR* incorporates the most complete atomic data base currently available for the modelling of X-ray spectra, it is also limited to densities below 10^{18} cm^{-3} .

At high densities, electrons in bound states require less energy to liberate them into the continuum than equivalent states in isolated atoms, because ions see the charge from neighbouring ions and electrons, which effectively depresses the ionization potential. This effect is called continuum lowering. Current calculations of ionization balance do not take this process into account in a comprehensive way. In our case, *XSTAR* contains a comprehensive and accurate treatment of continuum lowering for the H- and He-like isoelectronic sequences, and they are only applicable up to densities of 10^{18} cm^{-3} . Plus, *XSTAR* utilizes low-density recombination rates for ions from all other isoelectronic sequences, i.e. any ion with three or more electrons.

Three-body recombination is the inverse process of collisional ionization, and can affect all atomic levels given sufficiently high densities. It occurs when an electron approaches an ion with kinetic energy less than the binding energy of the recombined level, and that when second electron is within the same volume in order to carry away the liberated energy. This process is currently not included for all levels, but only to those excited levels most easily excited from the ground level by electron collisions. This is supplemented by those levels which can be populated by radiative recombination. As three-body recombination occurs preferentially to highly excited levels, the line emission from these levels can be strongly enhanced at high densities.

The emission of X-ray lines depends on the rates from many processes, including photoionization, radiative and di-electronic recombination, electron impact collisional excitation and ionization,

Auger decay and autoionization and bound–bound radiative decay. Plasma density can affect all of these, in principle, via effects of screening the nuclear charge on atomic structure. This can lead to rate coefficients which can be either larger or smaller than the low-density rates.

Stimulated processes will enhance the rates for recombination and radiative decay at high densities, and it is straightforward to include in the calculation of level populations. However, so far, *XSTAR* only includes this for recombination, given the current limitation to densities below 10^{18} cm^{-3} (i.e. stimulated processes become important at larger densities).

4 CONCLUSIONS

We have explored the effects of high densities on models of photoionized plasmas and reflection spectra. The primary effect of increasing the density is the suppression of line cooling near the disc’s surface, and the increase of free–free heating in the deeper regions, which results in an increase of the gas temperature. These effects, in turn, affect the ionization balance, typically increasing the ionization state of the gas as the density increases. The most obvious effect on the reflection spectrum is the increase of the thermal emission at low energies, which follows a Rayleigh–Jeans law. Additionally, the higher temperature also results in a higher ionization state, thereby affecting the emission line spectrum and continuum photoelectric absorption.

In the context of AGN, the enhanced emission at low energies could explain to some degree the soft excess observed in many sources. Higher densities might also explain the blackbody component that is required in fits to the spectra of extreme narrow-line Seyfert I AGN, such as 1H0707–495 (Fabian et al. 2009) and IRAS13224–3809 (Ponti et al. 2010), and possibly also fits to data indicating the presence of a second reflector with higher ionization identified by Dauser et al. (2012). Generally, the effects of high density are more dramatic for low-ionization state models.

High-density models are also important when the illumination of the inner disc is very strong. Specifically, for bright AGN, with the illuminating source near the black hole and moderate ionization, the density of the reflector is expected to exceed the typical densities

employed in standard reflection models (e.g. Parker et al. 2014; Kara et al. 2015).

As a first step, using our code `XILLVER`, we have produced a new library of reflection spectra that are publicly available.¹ The grid of models is for a single high value of the density, $n_e = 10^{19} \text{ cm}^{-3}$, while covering wide ranges of all the other relevant parameters (except for E_{cut} , which is fixed at 300 keV). This limited library of models is provided to enable individuals to test whether a high-density model of a peculiar source provides a better fit to the data than conventional reflection models. Ultimately, a large effort will be required to produce a comprehensive set of models that accurately describe the microphysics associated with the effects of high density. To a degree, we expect the density to be degenerate with the ionization parameter at some energies, though it may be possible to use the soft excess as a discriminator.

The atomic data currently available are somewhat incomplete and applicable only to plasma densities less than $n_e = 10^{19} \text{ cm}^{-3}$. This density limit imposes a serious limitation on our reflection models since the densities in BHB accretion discs are estimated to be significantly higher. Similarly, in other important environments, the densities are thought to be $>n_e = 10^{19} \text{ cm}^{-3}$, such as the accretion discs of neutron stars, the atmospheres of white dwarfs, and partially ionized outflows from galactic sources (Miller et al. 2015). At such densities, much of the rate data in current atomic data bases is inapplicable and new atomic calculations are sorely needed.

A principal use of reflection models is in estimating the spins of black holes where the fits to data are driven by the profile of the Fe K emission line and edge. Fits to the spectra of many sources have shown a clear correlation between the spin of the black hole and the abundance of Fe (Reynolds et al. 2012; Steiner & McClintock 2012). Moreover, the abundances are typically significantly greater than the solar value. The AGN 1H0707-495 is the most dramatic case with $A_{\text{Fe}} \sim 10\text{--}20$ (Fabian et al. 2009; Dauser et al. 2012). Meanwhile, supersolar abundances are also inferred in fitting high-quality spectra of BHBs such as Cyg X-1 (Parker et al. 2015) and GX 339-4 (Fuerst et al. 2015; García et al. 2015).

Because no concrete physical mechanism for extreme Fe enrichment has been identified,² it appears that there is a deficiency in the models. In current reflection models, it is the Fe-abundance parameter alone that controls the strength of the line emission. A possible explanation for the supersolar abundances is that current moderate-density models fail to include a significant line-production mechanism. It is imperative to explore this possibility by identifying and accurately including high-density plasma effects in computing atomic data, and then implementing these data in a new generation of reflection models.

The development of accurate high-density reflection models is now a priority given the high-resolution and pile-up-free data provided by *NuSTAR* (Harrison et al. 2013), and that *NICER* (Gendreau, Arzoumanian & Okajima 2012) will soon provide. The latter furthermore is sensitive down to ~ 0.2 keV, making their data ideal in searching for the predicted signatures of high-density plasma effects. These models are also relevant in broad-band AGN studies with current missions covering UV and soft X-rays such as *XMM-Newton*, particularly where the proper modelling of the soft X-ray

excess is important (e.g. Vasudevan & Fabian 2009; Jin, Ward & Done 2012; Petrucci et al. 2013; Mehdipour et al. 2015).

ACKNOWLEDGEMENTS

We thank the anonymous referee for their positive and useful comments, and Laura Brenneman for insightful discussions. JG and JEM acknowledge the support of a CGPS grant from the Smithsonian Institution. ACF acknowledges ERC Advanced Grant 340442 Feedback. JFS has been supported by the Einstein Fellowship grant PF5-160144.

REFERENCES

- Ballantyne D. R., 2004, *MNRAS*, 351, 57
 Ballantyne D. R., Ross R. R., Fabian A. C., 2001, *MNRAS*, 327, 10
 Bautista M. A., Kallman T. R., 2001, *ApJS*, 134, 139
 Cackett E. M. et al., 2010, *ApJ*, 720, 205
 Chen Z., Gou L., McClintock J. E., Steiner J. F., Wu J., Xu W., Orosz J., Xiang Y., 2015, *ApJ*, 825, 45
 Dauser T., Wilms J., Reynolds C. S., Brenneman L. W., 2010, *MNRAS*, 409, 1534
 Dauser T. et al., 2012, *MNRAS*, 422, 1914
 Dauser T., García J., Wilms J., Böck M., Brenneman L. W., Falanga M., Fukumura K., Reynolds C. S., 2013, *MNRAS*, 430, 1694
 Dauser T., García J., Parker M. L., Fabian A. C., Wilms J., 2014, *MNRAS*, 444, L100
 Dovčiak M., Karas V., Yaqoob T., 2004, *ApJS*, 153, 205
 Dumont A.-M., Collin S., Paletou F., Coupé S., Godet O., Pelat D., 2003, *A&A*, 407, 13
 Elvis M. et al., 1994, *ApJS*, 95, 1
 Fabian A. C., Ross R. R., 2010, *Space Sci. Rev.*, 157, 167
 Fabian A. C., Iwasawa K., Reynolds C. S., Young A. J., 2000, *PASP*, 112, 1145
 Fabian A. C. et al., 2009, *Nature*, 459, 540
 Felten J. E., Rees M. J., 1972, *A&A*, 17, 226
 Fuerst F. et al., 2015, *ApJ*, 808, 122
 García J., Kallman T. R., 2010, *ApJ*, 718, 695
 García J., Mendoza C., Bautista M. A., Gorczyca T. W., Kallman T. R., Palmeri P., 2005, *ApJS*, 158, 68
 García J. et al., 2009, *ApJS*, 185, 477
 García J., Kallman T. R., Mushotzky R. F., 2011, *ApJ*, 731, 131
 García J., Dauser T., Reynolds C. S., Kallman T. R., McClintock J. E., Wilms J., Eikmann W., 2013, *ApJ*, 768, 146
 García J. et al., 2014, *ApJ*, 782, 76
 García J. A., Steiner J. F., McClintock J. E., Remillard R. A., Grinberg V., Dauser T., 2015, *ApJ*, 813, 84
 Gendreau K. C., Arzoumanian Z., Okajima T., 2012, in Takahashi T., Murray S. S., den Herder J.-W. A., eds, *Proc. SPIE Conf. Ser. Vol. 8443, Space Telescopes and Instrumentation 2012: Ultraviolet to Gamma Ray*. SPIE, Bellingham, p. 844313
 Gou L. et al., 2014, *ApJ*, 790, 29
 Harrison F. A. et al., 2013, *ApJ*, 770, 103
 Jin C., Ward M., Done C., 2012, *MNRAS*, 422, 3268
 Kallman T., Bautista M., 2001, *ApJS*, 133, 221
 Kallman T. R., Palmeri P., Bautista M. A., Mendoza C., Krolik J. H., 2004, *ApJS*, 155, 675
 Kara E. et al., 2015, *MNRAS*, 446, 737
 Lawrence A., 2012, *MNRAS*, 423, 451
 McClintock J. E., Narayan R., Steiner J. F., 2014, *Space Sci. Rev.*, 183, 295
 Madej O. K., García J., Jonker P. G., Parker M. L., Ross R., Fabian A. C., Chenevez J., 2014, *MNRAS*, 442, 1157
 Mehdipour M. et al., 2015, *A&A*, 575, A22
 Mihalas D., 1978, *Stellar Atmospheres*, 2nd edn. Freeman, San Francisco, CA
 Miller M. C., Miller J. M., 2015, *Phys. Rep.*, 548, 1

¹ <http://hea-www.cfa.harvard.edu/javier/xillver/>

² Radiative levitation has been proposed by Reynolds et al. (2012) as a possible mechanism for the enhanced Fe abundances, but it has not yet been demonstrated through numerical calculations.

- Miller J. M., Fabian A. C., Kaastra J., Kallman T., King A. L., Proga D., Raymond J., Reynolds C. S., 2015, *ApJ*, 814, 87
- Mukai K., Rana V., Bernardini F., de Martino D., 2015, *ApJ*, 807, L30
- Nayakshin S., Kallman T. R., 2001, *ApJ*, 546, 406
- Noble S. C., Krolik J. H., Hawley J. F., 2010, *ApJ*, 711, 959
- Parker M. L. et al., 2014, *MNRAS*, 443, 1723
- Parker M. L. et al., 2015, *ApJ*, 808, 9
- Patrick A. R., Reeves J. N., Lobban A. P., Porquet D., Markowitz A. G., 2011, *MNRAS*, 416, 2725
- Petrucci P.-O. et al., 2013, *A&A*, 549, A73
- Plant D. S., Fender R. P., Ponti G., Muñoz-Darias T., Coriat M., 2015, *A&A*, 573, A120
- Ponti G. et al., 2010, *MNRAS*, 406, 2591
- Reis R. C., Fabian A. C., Ross R. R., Miniutti G., Miller J. M., Reynolds C., 2008, *MNRAS*, 387, 1489
- Reynolds C. S., 2014, *Space Sci. Rev.*, 183, 277
- Reynolds C. S., Nowak M. A., 2003, *Phys. Rep.*, 377, 389
- Reynolds C. S., Brenneman L. W., Lohfink A. M., Trippe M. L., Miller J. M., Fabian A. C., Nowak M. A., 2012, *ApJ*, 755, 88
- Ross R. R., 1979, *ApJ*, 233, 334
- Ross R. R., Fabian A. C., 1993, *MNRAS*, 261, 74
- Ross R. R., Fabian A. C., 2005, *MNRAS*, 358, 211
- Ross R. R., Fabian A. C., 2007, *MNRAS*, 381, 1697
- Ross R. R., Weaver R., McCray R., 1978, *ApJ*, 219, 292
- Rózańska A., Madej J., 2008, *MNRAS*, 386, 1872
- Rózańska A., Dumont A.-M., Czerny B., Collin S., 2002, *MNRAS*, 332, 799
- Sanders D. B., Phinney E. S., Neugebauer G., Soifer B. T., Matthews K., 1989, *ApJ*, 347, 29
- Schnittman J. D., Krolik J. H., Noble S. C., 2013, *ApJ*, 769, 156
- Shakura N. I., Sunyaev R. A., 1973, *A&A*, 24, 337
- Sobolewska M. A., Done C., 2007, *MNRAS*, 374, 150
- Steiner J. F., McClintock J. E., 2012, *ApJ*, 745, 136
- Steiner J. F., McClintock J. E., Orosz J. A., Remillard R. A., Bailyn C. D., Kolehmainen M., Straub O., 2014, *ApJ*, 793, L29
- Strüder L. et al., 2001, *A&A*, 365, L18
- Svensson R., Zdziarski A. A., 1994, *ApJ*, 436, 599
- Titarchuk L., 1994, *ApJ*, 434, 570
- Turner T. J., Pounds K. A., 1988, *MNRAS*, 232, 463
- Vasudevan R. V., Fabian A. C., 2009, *MNRAS*, 392, 1124
- Vasudevan R. V., Mushotzky R. F., Reynolds C. S., Fabian A. C., Lohfink A. M., Zoghbi A., Gallo L. C., Walton D., 2014, *ApJ*, 785, 30
- Walton D. J., Nardini E., Fabian A. C., Gallo L. C., Reis R. C., 2013, *MNRAS*, 428, 2901
- Zoghbi A., Fabian A. C., Uttley P., Miniutti G., Gallo L. C., Reynolds C. S., Miller J. M., Ponti G., 2010, *MNRAS*, 401, 2419
- Zycki P. T., Krolik J. H., Zdziarski A. A., Kallman T. R., 1994, *ApJ*, 437, 597

This paper has been typeset from a $\text{\TeX}/\text{\LaTeX}$ file prepared by the author.